

Microstructure-based modelling of isotropic and kinematic strain hardening in a precipitation-hardened aluminium alloy

G. Fribourg^a, Y. Bréchet^a, A. Deschamps^{a,*}, A. Simar^b

^a SIMAP, Grenoble INP—CNRS—UJF, BP 75, 38402 St. Martin d'Hères Cedex, France

^b MMC, Université catholique de Louvain, Louvain-la-Neuve, Belgium

Received 9 December 2010; received in revised form 18 February 2011; accepted 19 February 2011

Available online 21 March 2011

Abstract

This paper presents a study of the strain hardening of a 7000 series aluminium alloy. A wide variety of microstructural states are tested both in uniaxial tension and by performing Bauschinger tests. Their microstructural features are evaluated quantitatively in terms of precipitate size and volume fraction using small-angle X-ray scattering. A physically-based model for strain hardening, using a modified version of the Kocks–Mecking–Estrin formalism, is presented for the precipitation states that exhibit precipitate bypassing. The model takes explicitly into account the microstructural information and describes in detail the mechanisms governing the storage, stability and annihilation of Orowan loops around the precipitates. It describes both the uniaxial and the strain-reversal tests, by evaluating separately the kinematic and isotropic contributions to strain hardening and using an appropriate mixing law. In addition, the transient of strain-reversal Bauschinger tests is discussed with respect to the effect of precipitates on strain reversibility.

© 2011 Acta Materialia Inc. Published by Elsevier Ltd. All rights reserved.

Keywords: Aluminium alloy; Precipitation; Strain hardening

1. Introduction

The study of strain hardening in metals, namely the capacity of the material's flow stress to increase with increasing plastic strain, has attracted attention since the discovery of dislocations (see e.g. Refs. [1,2] for a review), and is still a matter of wide current interest, for example in solid solutions [3] or precipitates [4–12]. Understanding the strain-hardening capability of structural alloys is of practical importance since it controls in part their fracture properties, energy absorption and formability. Most of the commonly used finite-element software for engineering design use phenomenological constitutive laws, and there is widespread interest in the recent literature in developing simple but physically based constitutive laws that would rely on an understanding of the underlying mechanisms of plasticity. More fundamentally, strain hardening results

from the dynamics of the interaction of dislocations with each other and with the various constituents of the microstructure, which can be quite complicated in the case of engineering alloys—grain boundaries, precipitates and solutes to name a few. The associated dislocation storage processes may give rise both to directional back-stress (kinematic hardening) and to non-directional accumulation of obstacles to further dislocation motion (isotropic hardening).

A number of modelling tools are available to address the various aspects of the strain hardening of alloys. Atomistic modelling, such as molecular dynamics, is now capable of describing the interaction of dislocations with crystalline defects [13] as well as with precipitates [14–16]; however, the description of strain hardening to appreciable strains is well beyond the scope of current modelling. At the mesoscopic level, discrete dislocation dynamics (DDD) is now capable of describing the collective behaviour of dislocations in materials containing defects such as precipitates [17,18]. Although these models provide appreciable insight into the

* Corresponding author. Fax: +33 4 76 82 66 44.

E-mail address: alexis.deschamps@grenoble-inp.fr (A. Deschamps).

mechanisms of plasticity, they cannot as yet directly provide simple constitutive laws for strains corresponding to the uniform elongation of most metallic alloys. In order to do so, it is necessary to compute from DDD simulations the values of the parameters entering an “internal variable model”, and that has been done only for single crystals of pure metals [19].

A common approach for modelling the strain hardening of metals in a simpler way is to use internal variable models, based on the Kocks–Mecking–Estrin (KME) formalism [2,20–23]. This class of models has been initially developed for pure face-centred cubic metals based on the observation that the Taylor equation [24] (which states that the flow stress increment during plastic deformation is proportional to the square root of the dislocation density) holds in most situations. This model then describes the evolution of dislocation density (internal state variable) with strain, as a competition between storage and annihilation. It presupposes that isotropic hardening (storage of forest dislocations) dominates strain hardening. It is generally a good assumption in pure metals, except when the interaction with grain boundaries makes kinematic hardening more substantial. The one-internal variable version of the KME model provides a physical basis for Voce-type constitutive laws [25] and has been found to be in relatively good agreement with experimental data [2].

The addition of solutes to pure metals provides a first additional complexity in the formulation of strain-hardening models. It is usually observed to increase substantially the strain-hardening capability [3,26]. This effect was included in the KME model framework [23] by assuming that it was simply related to a change in the dislocation stacking fault energy, which controls dislocation dissociation, and thus their cross-slip ability and the dynamic recovery processes. However, most of the available experimental data do not agree with this simple picture [27–29]. Recent studies [30] suggest that solutes either change the strength of dislocation–dislocation interactions or the planarity of glide and thus the intensity of pile-up effects.

Precipitates also have a strong influence on strain hardening. This influence depends strongly on the nature of the dislocation–precipitate interactions, which can be broadly separated into two categories.

In the case where precipitates (coherent or semicoherent) are sheared by dislocations, one expects a low level of strain hardening associated with plastic localization [4,5,8,10,31]. However, few models exist that describe the strain hardening in such situations [23]. In this category, additional complexity can arise when the material’s solid solution is still supersaturated, in which case dynamic precipitation can occur during plastic straining [32,33]. At low temperatures dynamic precipitation is observed to cause high levels of apparent strain hardening, although the precipitates are shearable [34].

In the case of non-shearable precipitates, the strain-hardening rate is observed to be very large for small plastic strains [4,5,31], and is thought to result from the storage of Orowan loops around the second-phase particles. Two types of

descriptions are available in the literature for the effect of Orowan loop storage on strain hardening. This hardening can be described in terms of kinematic hardening by the accumulation of internal stresses caused by the elastic loading of the non-penetrable second-phase particles [35], or in terms of isotropic hardening by the accumulation of geometrically necessary dislocations acting as forest dislocations preventing further dislocation slip [36]. Elaborating the appropriate mixing laws between the contributions of strain hardening and that of the precipitates themselves has also been the subject of substantial research [4,6,18,37,38]. A quantitative model for strain hardening in these materials is in fact difficult to achieve, since it requires predicting the evolution of these internal stresses and dislocations with strain. When several Orowan loops are stored around a given particle, the high local levels of stress may cause spreading of the dislocations across the material, or shearing of the precipitates that were initially not penetrable by the dislocations [39]. Precipitate fracture under the effect of Orowan loops has also been reported [40].

Modelling of the strain hardening in presence of precipitates thus requires a number of ingredients (see Refs. [41,42] for reviews of existing models):

- (i) modelling the rate of storage of dislocation loops and build-up of internal stresses with strain, and how this saturates due to recovery mechanisms; and
- (ii) using the appropriate mixing laws between the different contributions to the flow stress, namely kinematic and isotropic hardening, and the contribution of dislocations and precipitates, as well as that of the solute atoms.

The separation of the kinematic and isotropic hardening components is traditionally investigated using strain-reversal tests that enable characterization of the Bauschinger effect [43]. These tests are very sensitive to the details of the dislocation–precipitate interactions [44], and are also a valuable tool to understand the transition between different modes of interaction (such as the shearing-to-bypassing transition). However, the behaviour of precipitate-hardening materials upon strain reversal is quite complex, showing extensive strain transients with characteristics that depend on the microstructure and on the level of the forward strain [40].

In the current state of the art, the existing literature provides now well-established models on the one hand for predicting the monotonic hardening in precipitation hardening materials whose particles undergo Orowan bypassing [5], and on the other hand of the build-up of internal stresses as characterized by stress-reversal Bauschinger experiments [40]. However, little literature exists that encompasses both phenomena into a comprehensive model, whose predictive capability would be able to extend to strain path changes. One notable exception is the recent work by da Costa Teixeira et al. [8] in Al–Cu–Sn alloys, for the case of shear-resistant θ' precipitates.

The aim of the present paper is first to establish a corpus of data about monotonic strain hardening and the Bauschinger effect, together with a quantitative analysis of the precipitate microstructure, in a classical precipitation-hardening system. The Al–Zn–Mg–Cu system serves this purpose well. It is a widely used material for aerospace applications [45] and presents a very large strengthening response. It has a well-defined peak strength, usually associated with a shearing-to-bypassing transition [46]. The hardening precipitates in this system, although not spherical, have a moderate aspect ratio as compared to other aluminium alloys [47].

A model will then be presented that provides a single framework for modelling the monotonic stress–strain curve and the Bauschinger effect. This model combines the prediction of isotropic hardening by Simar et al. [5] and of kinematic hardening by Proudhon et al. [40] with appropriate mixing laws. It is microstructure-based and will explicitly take into account the microstructural parameters measured in the first part. One limitation of this model is that no attempt is made to describe the strain transient of the Bauschinger effect. However, a phenomenological description of the magnitude of this transient will be proposed.

2. Materials and experimental methods

2.1. Material and heat treatments

The studied material is an AA7449 alloy. The composition in the main alloying elements of the specific received plate, provided by Alcan, Centre de Recherches de Voreppe, France, was 8.3% Zn, 2.2% Mg and 1.9% Cu (wt.%). This material exhibits a relatively large grain size (50–200 μm), with a fibrous structure (subgrain size of approximately 3 μm). This grain and subgrain structure is fully stable at the ageing temperature.

The as-received temper was T7651, i.e. pre-strained and over-aged. The industrial ageing treatment consists of a water quench from the solution treatment temperature, a plastic deformation of about 0.02, a few days of natural ageing, and a two-step ageing treatment: 6 h at 120 °C and 10 h at 160 °C. In order to study precipitation microstructures with very large precipitates, samples of the T7651 temper were over-aged at 210 °C for different times. These tempers will be labelled “T7651 + Xd” in the following, where X stands for the number of days of ageing at 210 °C.

Most of the studied alloys were prepared according to a model heat treatment that did not include the plastic deformation before ageing, so that the resulting microstructures would have the lowest possible initial dislocation density before straining. The heat treatment consisted in a solution treatment at 474 °C, a cold water quench, natural ageing for 4 days, ageing at 120 °C for 6 h (heating ramp 30 °C h⁻¹), followed by ageing at 160 °C for various times up to 1000 h (heating ramp 15 °C h⁻¹). These samples will

be labelled “MXh” in the following, where X stands for the number of hours of artificial ageing, starting at the beginning of the ramp from room temperature to 120 °C.

2.2. Characterization of the microstructure

The precipitate microstructure has been mainly evaluated using small-angle X-ray scattering (SAXS) with the objective of obtaining quantitative measurements of the precipitate size and volume fraction with the heat treatment. Compared to transmission electron microscopy (TEM), SAXS measurements provide information averaged over a much larger amount of material, and this technique is therefore better adapted to the determination of average values of the microstructural parameters. Dumont et al. [47] have shown that in a similar but less concentrated alloy, SAXS offers reliable measurements of the precipitate size and volume fraction. In addition to the comparison made in Ref. [47] between SAXS, TEM and atom probe, which justified the use of the Guinier radius for the characterization of an average precipitate size, recent calculations [48] have shown that in the case of a polydisperse distribution of particles of moderate aspect ratio, the measured Guinier radius provided an estimate of the average particle radius within a precision better than 10%. On the other hand, the calculation of the precipitate volume fraction by SAXS needs to assume a certain precipitate composition. In the present case, a composition containing 33% Mg, 10% of Al and 57% Zn + Cu was assumed, in line with the results of Refs. [47,49] for over-aged microstructures. Given the possible uncertainty on this composition, the precision on the volume fraction measurement can be estimated to $\pm 10\%$. The small-angle scattering experiments were carried out both on a laboratory rotating anode (Cu K α source) and at the European Synchrotron Research Facility (ESRF) on the BM02/D2AM beamline, at a wavelength of 0.13 nm, for the microstructures containing the largest precipitates, where a higher resolution in scattering vector was needed. CCD camera data were corrected for read-out noise, distortion, flat-field, background noise, and were then normalized using a reference sample and transmission measurements through calibrated filters. From the radial averaged data, the precipitate size and volume fractions were calculated using the Guinier radius and the integrated intensity, in the same way as in Ref. [47].

2.3. Tensile and Bauschinger tests

Tensile tests were carried out using a screw-driven Zwick apparatus with a 20 kN load cell. The sample cross-section was 3 mm \times 5 mm, and the gauge length 60 mm. The strain rate was 10⁻³ s⁻¹.

Bauschinger tests were carried out using a hydraulic MTS machine with hydraulic wedge grips for cylindrical specimens of 12 mm diameter and a load cell of 100 kN. The gauge section was 8 mm in diameter and the gauge length 15 mm in length, so as to avoid buckling during

the compression tests. The extensometer gauge length was 10 mm. Heat treatments were carried out before machining the Bauschinger samples so that no distortion could alter the sample geometry between machining and testing. Tests were carried out first in tension and then in compression. The strain rate was 10^{-4} s^{-1} . It was checked by comparing the forward curve of the Bauschinger tests and the full tensile curve that the difference in flow stress caused by this strain-rate difference was negligible, due to the low strain-rate sensitivity of this alloy.

3. Precipitation kinetics

Fig. 1 shows the evolution of the precipitate parameters during artificial ageing. During the first heating ramp that brings the material from room temperature to 120°C , the particle number density is observed to decrease by an order of magnitude, together with an increase in particle size and a small decrease in volume fraction. This transition is classically related to the reversion of the pre-existing Guinier–Preston (GP) zones [50]. During ageing at 120°C a growth stage is observed with an almost constant precipitate number density, an increasing radius and an increasing volume fraction. The second ramp to 160°C results again in a substantial decrease in the precipitate number density, accompanied by a small decrease in volume fraction and a large increase in radius. During this stage, the transition between the GP zones and the η' precipitates takes place as evidenced from the in situ SAXS data by the change from an isotropic signal characteristic of the GP zones (that are known to be spherical in this system [51]) to an anisotropic signal characteristic of the η' platelets. This transition is known to occur by nucleation of the η' phase on the dissolving zones [51,52]. Subsequently, at 160°C the precipitate size grows steadily while the volume fraction stabilizes, which is characteristic of the precipitate coarsening stage. Transition from η' to η precipitates is presumed to occur during this ageing step [53], but does not result in any specific signature in terms of precipitate growth rate or volume fraction. It is therefore likely that the transition from the metastable to the stable precipitate is very progressive. For a comprehensive review of precipitation processes in 7000 series aluminium alloys, see Ref. [54].

Fig. 2 summarizes the microstructures at different stages of the precipitation treatment, compared to that of the T7651 temper, and to that of the samples over-aged to 210°C . A very wide range of precipitate sizes is obtained, from 1.6 nm η' to 26 nm η particles. Fig. 3 shows a TEM micrograph of the M45h temper (over-aged) and an associated diffraction pattern, which evidences (according to the indexing procedure that can be found, for example, in Ref. [53]) that the precipitates present at this stage are mainly of the stable η phase.

This range of precipitate microstructures, whose parameters are now quantitatively known, will serve as a basis for the understanding of the strain-hardening behaviour.

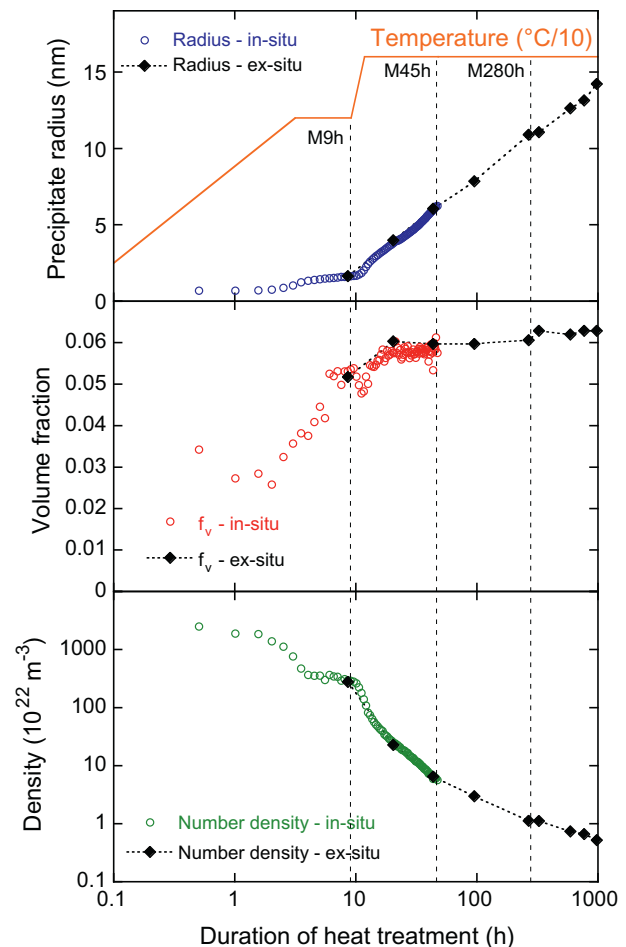


Fig. 1. Evolution of the precipitate parameters during the two-step heat-treatment measured by small-angle X-ray scattering. In situ measurements were made on one sample heated under the X-ray beam, while ex situ measurements were made on samples heat treated in a separate furnace and then measured. An estimate of the precipitate number density is calculated using $N \approx 3f_v/4\pi r$, where f_v is the volume fraction and r the radius of the precipitates. Some specific ageing times are specified in the graph, corresponding to samples studied in more detailed by mechanical tests. The relative precision on the measurement of precipitate radiuses and volume fractions is estimated to $\pm 10\%$. As a result, the precision on the precipitate number density is within $\pm 40\%$.

4. Mechanical tests

4.1. Tensile tests

Fig. 4 shows the tensile stress–strain curves during the different stages of the heat treatment, separated into two groups for clarity: under-aged samples in the first, and over-aged samples in the second (the peak-aged temper is represented in both cases).

The naturally aged material (M0h) possesses a yield strength of about 360 MPa associated with a high strain-hardening capability. During the first 12 h of ageing (i.e. before reaching the temperature of 160°C), the yield strength increases steadily without too much change in the strain-hardening behaviour. When the 160°C heat

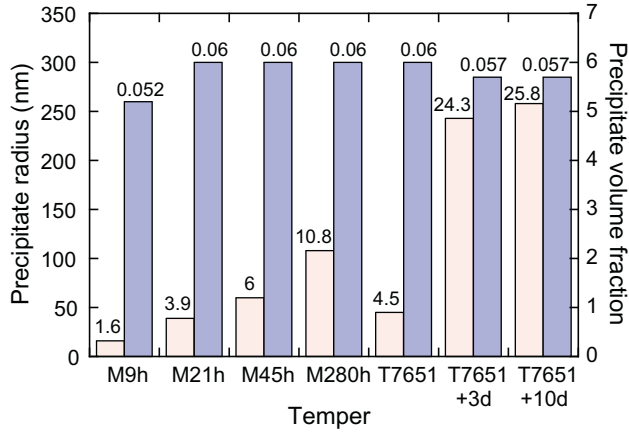


Fig. 2. Summary of precipitate sizes and volume fractions for the different stages of the model heat treatment and of that of the T7651 temper and over-aged tempers, which correspond to the heat treatments of the main mechanical tests presented subsequently.

treatment stage is reached, however, the strain-hardening rate suddenly changes to a new characteristic behaviour, associated with the material's peak strength. Another change in behaviour occurs progressively during over-ageing, with an increasingly high strain-hardening rate at small strains together with a rapidly saturating flow stress at larger strains.

For substantially over-aged samples, an inflexion point appears in the stress–strain curve, similarly to what has been widely reported in the literature in, for example, Al–Zn–Mg [4,31], Al–Mg–Si [5,40,55] and Al–Sc [6] alloys.

A more precise evaluation of the strain-hardening response is obtained by representing the data in the Kocks–Mecking plots (strain-hardening rate $\theta = d\sigma/d\varepsilon$ vs. stress–yield stress) (see Fig. 5). The strain-hardening behaviour can be separated in three groups of curves, as follows:

- Under-aged samples, where the strain-hardening rate is quite similar to that of the naturally aged material. The strain-hardening rate has a high initial value, and slowly decreases with increasing flow stress (from M0h to M12h).
- Samples close to peak strength, whose strain-hardening rates are extremely low. Their initial value of strain hardening is low and the decrease is rapid (M14h to M22h).
- Over-aged samples, whose strain-hardening rate is substantially larger, notably in the initial part of the deformation (M45h onwards and T7651).

It is striking that the transition from the second group to the third group coincides quite precisely with a drop in the peak strength of the alloy, which corresponds to the shearing/bypassing transition.

We have seen in the Introduction that these curves are classically discussed within the KME model framework, where in the case of pure metals they are supposed to be linear (see Eq. (3) in Section 5). Although there is no reason for the strain-hardening curves to be linear in the case of materials containing precipitates, a linear part is usually found in between the steep decrease from the elastic modulus characteristic of the elastic-to-plastic transition and the sharp decrease characteristic of the occurrence of necking. Thus, one can associate with a strain-hardening curve two parameters, i.e. the extrapolated initial strain-hardening rate θ_0 and the steady-state rate of decrease of the strain-hardening rate with respect to stress (in absolute value) $\beta_0 = -d\theta/d\sigma$, as has been done, for example, in Refs. [4,5,10]. This linear relationship between the current work-hardening rate and the flow stress in excess of the yield stress does not hold for the elastic–plastic transition (when the grains are progressively yielding), or in the post-necking region (when the strain becomes localized). Thus the range to calculate

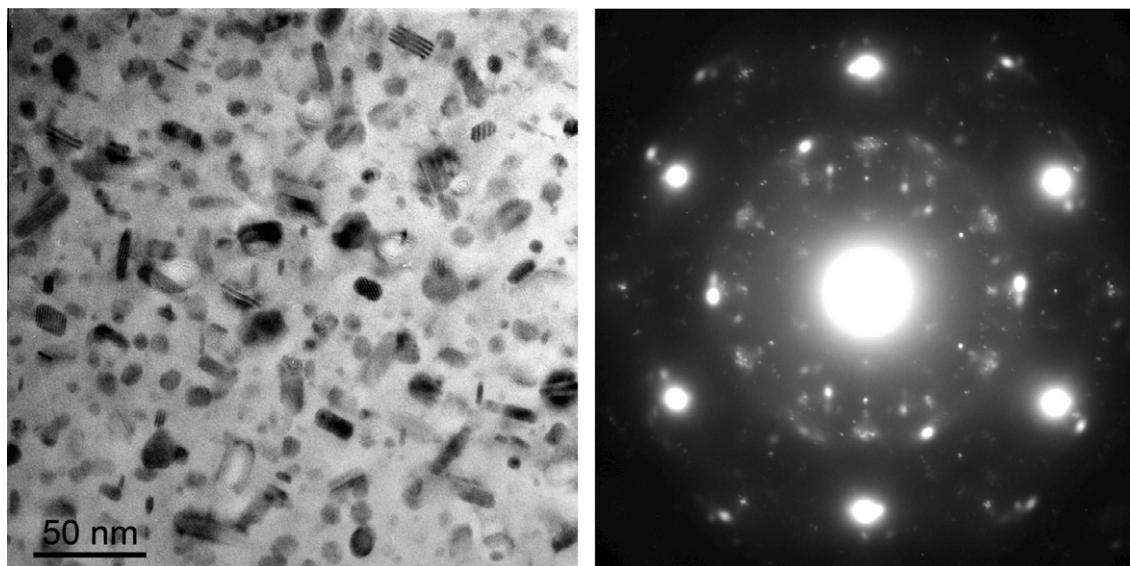


Fig. 3. TEM micrograph of the material aged 45 h (M45h), and associated $\langle 111 \rangle$ Al diffraction pattern.

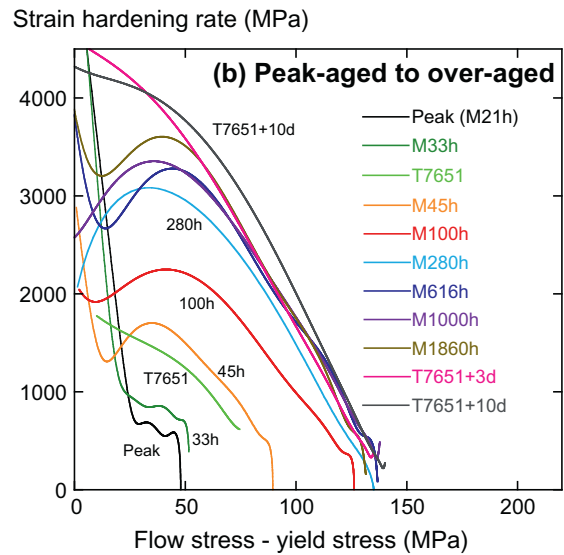
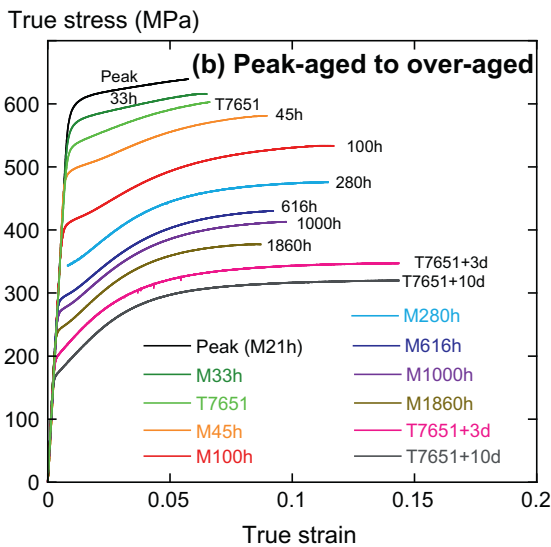
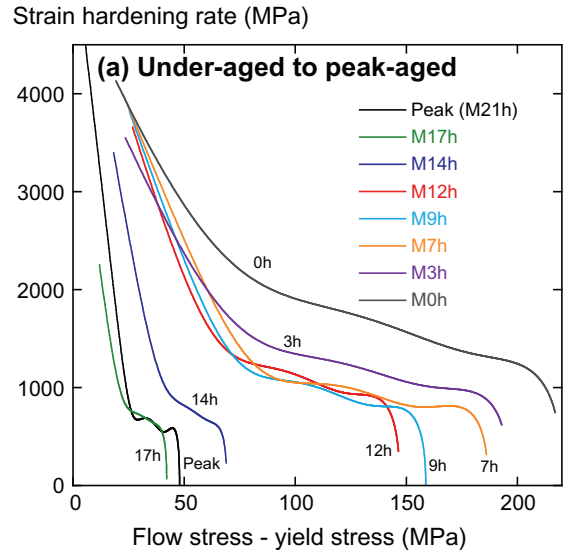
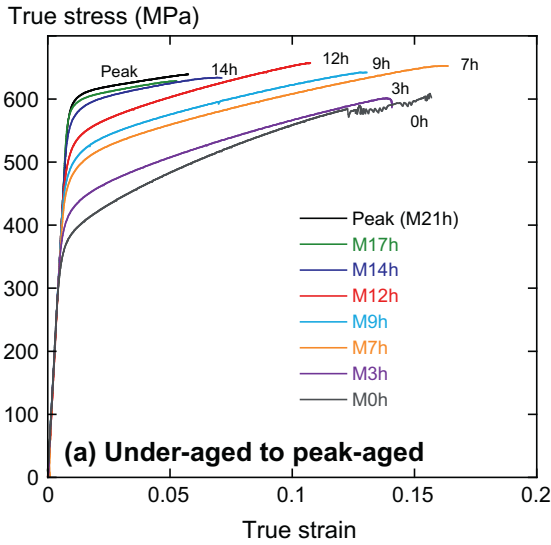


Fig. 4. Tensile curves for different times along the ageing treatment: (a) under-aged to peak-aged tempers; (b) peak-aged to over-aged tempers.

Fig. 5. Strain-hardening curves for different times along the ageing treatment: (a) under-aged to peak-aged tempers; (b) peak-aged to over-aged tempers.

the θ_0 and β_0 parameters is about 100 MPa (depending on the heat treatment), as shown in Fig. 5.

Fig. 6 shows the evolution of these parameters during the ageing treatment, along with the evolution of yield strength and ultimate tensile strength. It makes it possible to quantify the discussion on the evolution of strain hardening for the different microstructures:

- The initial hardening rate θ_0 is observed to be high (between 2000 and 3000 MPa) and to decrease during the first stages of artificial ageing. It reaches a value characteristic of pure aluminium (about 1200 MPa or $\mu/20$) at the material's peak strength (precipitate radius of 3.9 nm). During this stage, the rate of decrease of the strain-hardening rate β_0 is found to be constant.
- After the peak strength is reached, two phenomena occur suddenly. First, the parameter β_0 suddenly increases, and subsequently a similar increase happens

with the initial strain-hardening rate θ_0 . For the longest stages of ageing investigated here, the initial hardening rate reaches very high values of about 6000 MPa. According to the common interpretation of such curves made in the literature (e.g. [5]), the increase in θ_0 is characteristic of the transition between shearing and bypassing of particles, whereas the change in β_0 results in a more complicated manner from the effect of Orowan loops on dynamic recovery. What supports this first association is the fact that the change in θ_0 occurs at the peak strength, which is generally attributed to the shearing-to-bypassing transition for the interaction between dislocations and precipitates in 7000 series Al alloys [54]. The evolution of β_0 and θ_0 are very similar to that of 6000 series Al alloys [5] except that in the latter case the shearing-to-bypassing transition is not

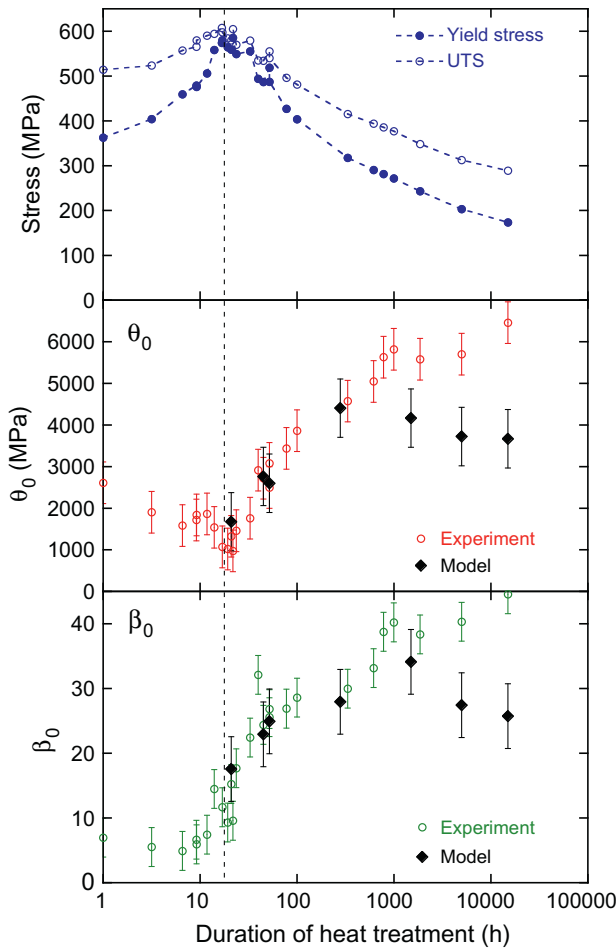


Fig. 6. Evolution of the yield stress (± 5 MPa), ultimate tensile stress (± 10 MPa) and strain-hardening-parameters β_0 and θ_0 with ageing time, measured by linear fitting from the strain-hardening curves in Fig. 5. The black diamond symbols represent the values found from the model that is presented in Section 5.

necessarily associated with the peak strength [55] and a decrease of both parameters for massive over-ageing is observed that does not happen here.

4.2. Bauschinger tests

Tension–compression Bauschinger tests were performed for selected ageing times that were chosen to be representative of the most important stages identified on the tensile curves (see Fig. 2 for the corresponding microstructures). Experimental results for these tests will now be presented. First a comparison will be shown between the tensile tests and the compression reversals, for various values of imposed plastic strain during the tensile test (forward plastic strain ε_{FPS}). Then we will present the evolution of the internal stress level $\langle \sigma \rangle$ (equal to half the difference between the stress value at maximum forward strain and the reverse stress value; see Eq. (1) for the different microstructures:

$$\langle \sigma(\varepsilon_{\text{RP}}) \rangle = \frac{\sigma_{\text{F}}(\varepsilon_{\text{FP-max}}) - |\sigma_{\text{R}}(\varepsilon_{\text{RP}})|}{2}. \quad (1)$$

Here $\sigma_{\text{F}}(\varepsilon_{\text{FP-max}})$ is the maximum flow stress in tension before compression is applied, and $\sigma_{\text{R}}(\varepsilon_{\text{RP}})$ is the reverse (compression) flow stress at the reverse plastic strain ε_{RP} .

Fig. 7 shows the forward and reverse stress–strain curves for selected ageing conditions corresponding to one under-aged temper (M9h), the peak ageing temper (M21h), and several over-aged tempers. What one would expect, if there was no Bauschinger effect, is a reverse loading curve following exactly the tensile curve: the stress–strain curve should be independent of the strain path. This is obviously not the case here, which can be identified as a Bauschinger effect.

The first feature of this Bauschinger effect is that the yield stress during reverse loading is not equal to the maximum flow stress reached during forward loading. The general behaviour is then the following: a steep transient where the strain-hardening rate in compression is much higher than that of tension at the same plastic strain, and then an asymptotic behaviour where the compression and tensile curves become parallel, with or without a residual difference in flow stress.

This general behaviour depends on the temper. If all the over-aged materials exhibit more or less the same behaviour, the under-aged material (M9h) recovers its mechanical properties more rapidly during reverse loading. This lower Bauschinger effect for under-aged states was also reported in Ref. [40] for a 6000 series Al alloy.

This behaviour also varies with the initial forward strain level. For the samples that had experienced the smallest amount of forward strain, an inflexion point can be observed in the middle of the reverse part; it disappears for larger forward plastic strains (here, at about 0.03). Similar observations have been found in the literature [40,56].

Various reverse strain offsets have been used in the literature to define a stress characteristic of the Bauschinger effect; classically between 0.001 [44] and 0.02. We show the influence of the offset value in Fig. 8. The general behaviour is the same: the measured internal stress increases up to a certain value of the forward strain (about 0.02–0.03), after which $\langle \sigma \rangle$ saturates. However, the chosen reverse offset value affects strongly the order of magnitude of the Bauschinger stress (up to a factor of three difference).

This material thus exhibits a strong Bauschinger effect, which depends both on the forward strain level and the material temper. This complex behaviour may be described using three parameters [56]:

- The first parameter illustrates the reduction of yield stress during reverse loading, and is defined as the level of internal stress for 0.001 reverse plastic strain ($\langle \sigma(\varepsilon_{\text{RP}} = 0.001) \rangle$), relative to the yield stress (see Fig. 9a). The choice of $\varepsilon_{\text{RP}} = 0.001$ represents well the microplastic yield stress.
- The second parameter illustrates the steady-state internal stresses, and is defined as the level of internal stress for 0.02 reverse plastic strain ($\langle \sigma(\varepsilon_{\text{RP}} = 0.02) \rangle$), relative to

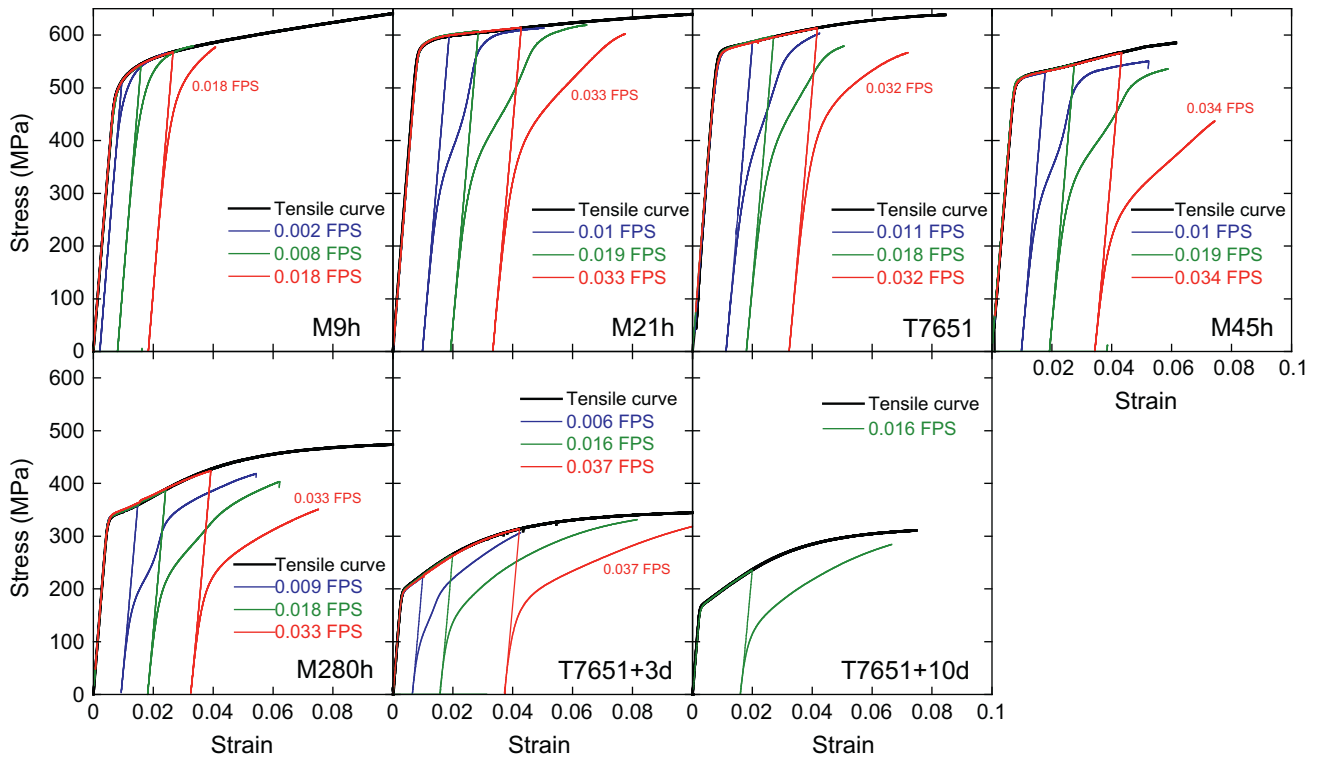


Fig. 7. Tensile curves, as well as reversed compression tests following different values of the forward plastic strain (FPS) for the seven selected states of ageing whose microstructural parameters are presented in Fig. 2.

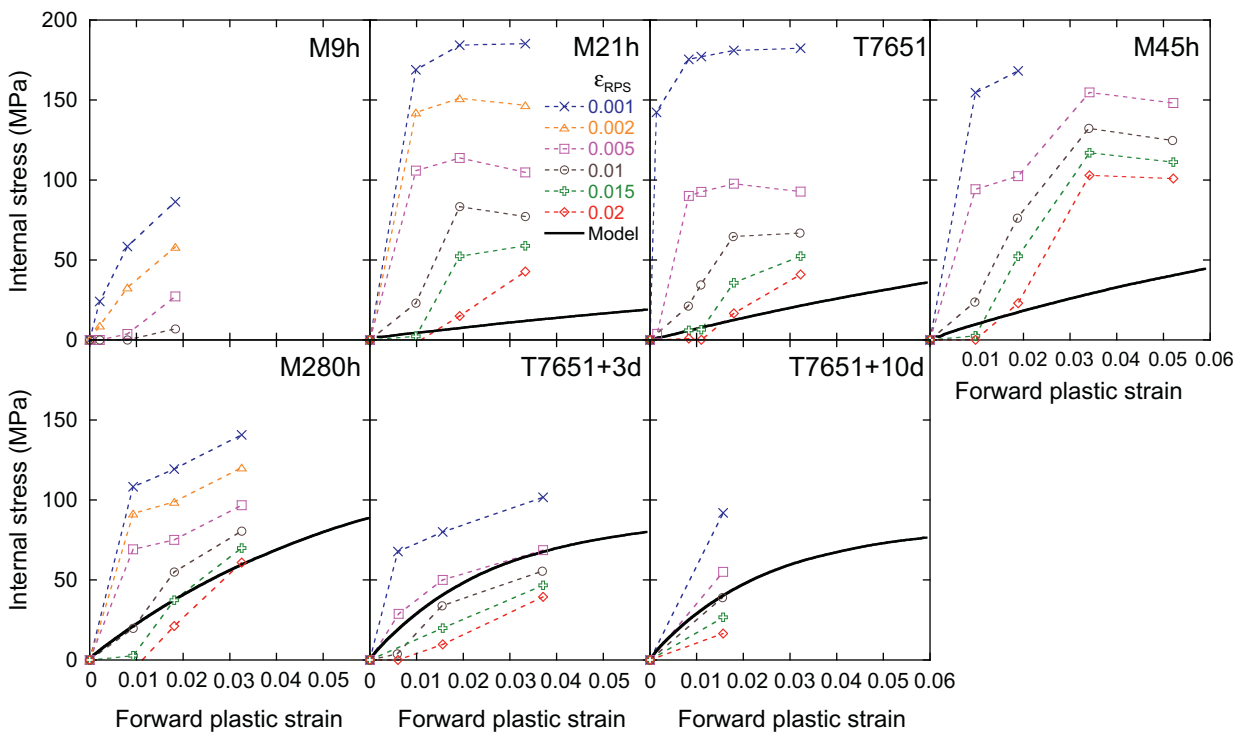


Fig. 8. Evolution of internal stress (as defined by Eq. (1)) as a function of forward plastic strain for the selected microstructures of Fig. 7. The internal stress is calculated for different values of the reverse plastic strain ϵ_{RPS} , between 0.001 and 0.02, as indicated for the different curves. The continuous lines correspond to the outcome of the model presented in Section 5 for the kinematic contribution to strain hardening. The error bars on the data reported on these graphs were estimated by repeating some of the experiments to $\pm 10\%$ (relative).

the yield stress (Fig. 9b). $\varepsilon_{RP} = 0.02$ has been chosen to overtake the inflexion point, generally present before 0.02 plastic strain.

- The third parameter illustrates the strain necessary to reach the steady-state internal stress, and is defined as the reverse plastic strain necessary to reach the same stress as before reversal: $\varepsilon_{RP-eq} = \varepsilon_{RP}(\sigma_R = \sigma_{F-max})$ (Fig. 9c).

The large magnitude of the difference between the forward and reverse yield stresses indicates that reverse loading is clearly favoured, which at first sight is indicative of a large kinematic contribution to work hardening. However, this range of internal stresses (50–200 MPa) greatly exceeds the value of strain hardening during the forward plastic straining and is thus too high to correspond to the back-stress simply due to the storage of Orowan loops (expected order of magnitude: 10–50 MPa). A possible interpretation, in line with the initial suggestion by Gould and co-workers [57], is that dislocation glide is partly reversible: the mobile dislocations follow (at least partially) the same path during forward loading and reverse loading, but in opposite directions.

In this case, the Orowan loops stored around the non-shearable precipitates during forward straining are annihilated by the mobile dislocations with opposite Burgers vector following the reverse path. This mechanism is illustrated in Fig. 10. It happens, for instance, to the dislocation labelled “2”; During the first steps of reverse loading, the non-shearable precipitates are therefore “transparent” to the mobile dislocations and do not contribute to the flow stress, since the moving dislocations annihilate the loops and do not have to exert a force to bypass the particle. We call this mechanism “Orowan loop helped reverse bypass” (OHRB). If the glide was 100% reversible in a

material with non-shearable precipitates, the reverse strain necessary to reach the maximum forward flow stress (i.e. when all the forward loops have been cancelled) would be $\varepsilon_{RP-eq} = 2\varepsilon_{FP-max}$. One may see it simply as follows: after one ε_{FP-max} in the reverse direction, all the loops are annihilated (OHRB effect) and an extra ε_{FP-max} is required for the dislocation structure to recover its situation before reversing the load. One can see on Fig. 9c that this relation is actually valid up to ~ 0.02 of forward plastic strain for the over-aged materials. On the contrary, ε_{RP-eq} is much lower than $2\varepsilon_{FP-max}$ for the under-aged M9 h material: it recovers its original flow stress sooner after reversal. As it contains very few non-shearable particles, there is almost no OHRB.

The anomalously large value of the apparent internal stress calculated with 0.001 reverse plastic strain for the over-aged materials can be thus explained by invoking the OHRB mechanism. The saturation of this internal stress with forward plastic strain can also be understood qualitatively by two arguments: firstly, the number of loops that are stored around precipitates saturate, so that the level of reverse strain that can happen before the remaining loops are all cancelled saturates as well; secondly, one can expect that at larger strains the Orowan loops stored around the precipitates experience cross-slip and become non-recoverable, and in addition the longer the path of the moving dislocation, the more likely a cross-slip event is to occur, preventing a backward motion along the same glide plane. Both effects are limiting thereby the OHRB mechanism. The larger the precipitates, the larger is the magnitude of this saturation internal stress (see Fig. 9a). This is consistent with an increased ability for large precipitates to store Orowan loops and a decreasing ability for the loops stored around large precipitates to change slip plane via a recovery mechanism.

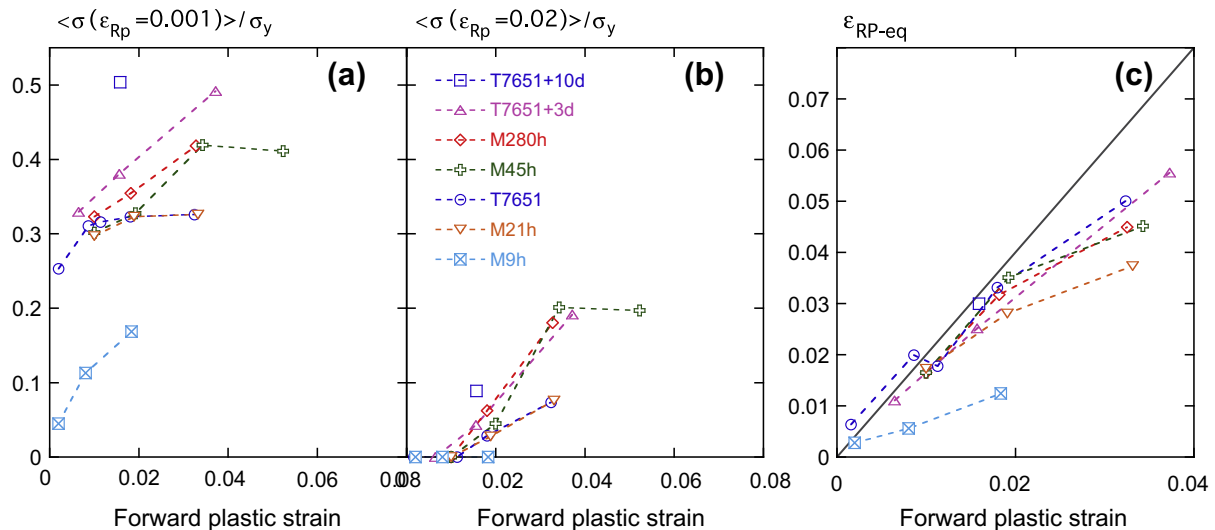


Fig. 9. (a) Evolution of the reduction in reverse yield stress (measured by the internal stress at 0.001 reverse plastic strain (see Eq. (1)) reduced by the forward yield stress for the different tempers investigated; (b) evolution of the reverse internal stress at 0.02 reverse plastic strain reduced by the forward yield stress for the same materials; (c) evolution of the reverse plastic strain necessary to reach the same stress level as reached during forward loading for the same materials.

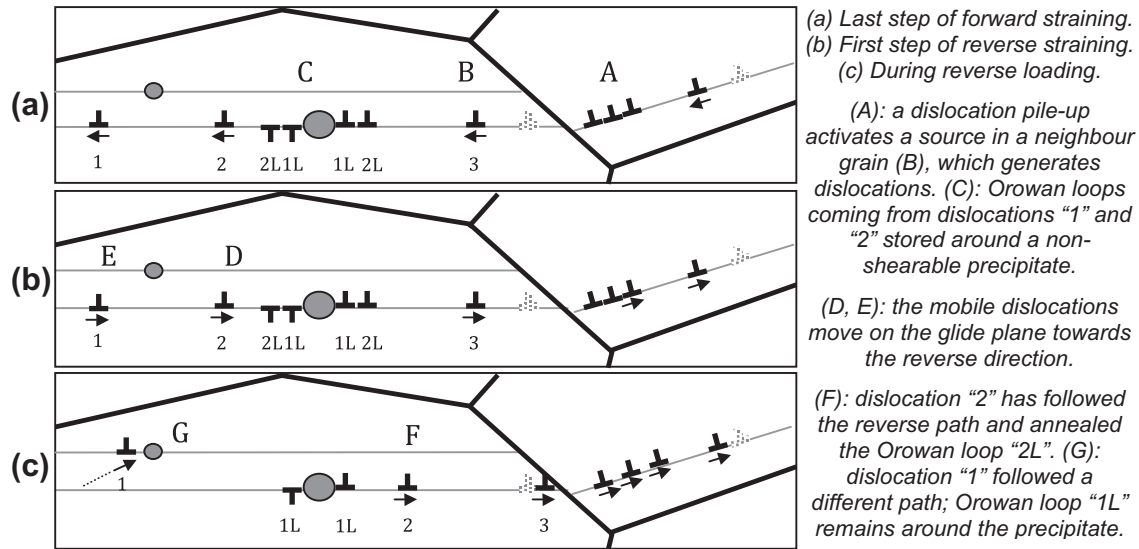


Fig. 10. Scheme describing the "Orowan loop helped reverse bypass" (ORHB) mechanism: (a) dislocation motion during forward straining; (b) the very beginning of reverse straining; (c) a later stage of reverse straining.

5. Model for strain hardening

The experimental results, presented in Section 4, evidence the major impact of the precipitation state on the strength and strain hardening of this age-hardenable aluminium alloy. The aim of the present model is to predict this influence based on microstructural parameters: the initial dislocation density, the remaining solute, the precipitate radius and volume fraction. In terms of strain hardening, the model focuses on over-aged conditions giving rise to Orowan looping while straining. In addition, the OHRB will be quantified using the internal stresses predicted by the model.

5.1. Model description

The KME model gives the evolution of the density of statistically stored dislocations (i.e. excluding Orowan loops) ρ_s with the plastic strain ε_p in a precipitate-free material:

$$\frac{\partial \rho_s}{\partial \varepsilon_p} = M(k_1 \sqrt{\rho_s} - k_2 \rho_s), \quad (2)$$

where M is the Taylor factor, k_1 is associated with the rate of dislocation storage, and k_2 with the rate of dynamic recovery. If no Orowan loops are stored in the material, the strain-hardening rate $\theta = d\sigma/d\varepsilon$ evolution can be deduced from Eq. (2) and the Taylor relationship $\sigma = M\alpha Gb\sqrt{\rho}$:

$$\theta = \theta_0 - \beta_0(\sigma - \sigma_y), \quad (3)$$

where ρ is the total dislocation density, α is a constant, G is the shear modulus, σ_y is the initial yield stress, $\theta_0 = M^2\alpha Gbk_1/2$ and $\beta_0 = Mk_2/2$. This is the derivative form of the classical Voce relation.

When the radius of the precipitate is larger than the radius of transition between precipitate shearing and precipitate bypassing, R_{trans} , Orowan loops are stored around precipitates during plastic deformation. Those loops are not always stable. Different mechanisms can explain self-annihilation, such as dislocation cross-slip or shearing of the precipitate by an initially stored dislocation due to an increase of the exerted stress by subsequent stored loops [39]. Hence an efficiency factor φ of the loop storage is introduced [5]. When precipitates are shearable (i.e. $r < R_{trans}$), no Orowan loops are stored by dislocation bypassing and hence φ is equal to 0. When the precipitates grow, the efficiency of Orowan loop storage increases. When the precipitates become incoherent with the aluminium matrix (i.e. when $r \geq R_{trans2}$), no more Orowan loop recovery is possible, and the efficiency φ is equal to 1. In between these two cases, for the sake of simplicity φ is assumed to increase linearly with precipitate radius from $r = R_{trans}$ to $r = R_{trans2}$.

When Orowan loops are stored around precipitates, k_2 depends on the precipitate size and volume fraction expressed in terms of critical annihilation distance between two moving dislocations y (interplane distance) [26], i.e. $k_2 = 2y/b$. The value of y depends on the configuration: if the lattice is strongly strained by the presence of a dislocation loop stored around a non-shearable precipitate located in between the moving dislocations, the annihilation distance is larger (i.e. annihilation happens more easily) than when no obstacle is standing between the two dislocations. Indeed, the stress field associated with the presence of Orowan loops favours cross-slip of mobile dislocations occurring nearby, effectively increasing the annihilation distance. The probability of two moving dislocations annihilating without being "helped" by a precipitate surrounded by at least one Orowan loop is equal to $\exp(-l_0\varphi/L)$ [5],

where l_0 is the mean distance between two moving dislocations and L is the mean distance between precipitates. L is given by Friedel's formalism as $L = r\sqrt{2\pi/3f_v}$ [58]. k_2 can be expressed as the sum of a first term, taking into account the proportion of the dislocations from the matrix which annihilate in pairs in the case where only these two dislocations are involved in the annihilation process (associated with the constant k_2^0) and a second term, taking into account the dislocations which annihilate in pairs due to the interaction with a dislocation loop efficiently stored around a non-shearable precipitates (associated with the constant k_2^p) [5]:

$$k_2 = k_2^0 \exp\left(-\frac{l_0\phi}{L}\right) + k_2^p \left[1 - \exp\left(-\frac{l_0\phi}{L}\right)\right], \quad (4)$$

where l_0 is equal to $\rho_s^{-1/2}$. Hence, the derivation of ρ_s implies solving the differential equation given by Eqs. (2) and (4).

In Proudhon et al.'s model [40], the number of loops n which can be stored around precipitates is related to the plastic strain through an expression that leads to the saturation of the Orowan loops number at n^* :

$$\frac{\partial n}{\partial \varepsilon_p} = M \frac{2r}{b} \left(1 - \frac{n}{n^*}\right). \quad (5)$$

This equation has been used to describe the effect of grain size on work hardening [59], as well as the precipitate contribution to kinematic hardening [60]. The “geometrically necessary dislocation term” $2r/b$ would lead to an unbounded increase in the polarised stresses, linearly increasing with strain. This cannot be possible for physical reasons: relaxation processes will be activated when the local stress increases, either by relaxation at the interfaces, by particle penetration, or by punching-off secondary dislocations. These mechanisms limit the development of internal stresses. The term $(1 - n/n^*)$ clearly has the correct behaviour for $n = 0$ and leads to a saturation toward a maximum number of stored dislocations n^* . The physical origin for n^* can be interpreted as a maximum number of storage sites. If dislocations were arriving at random on the particle, the linear expression would be rigorous, simply translating a “probability of arriving on an unoccupied site”. Of course, the dislocations arriving on the particle are likely to be somewhat correlated (since they come from a finite number of sources), so that the linear expression is likely to over-evaluate the probability of storage: this could easily be accounted for via an exponent $(1 - n/n^*)^p$, with $p > 1$. However, we have chosen to keep the linear expression, first to limit the number of adjustable parameters, and second due to the fact that the number of sources is likely to be less numerous than the number of precipitates, and the random arrival on a precipitate is therefore most probably a reasonable assumption.

This equation also means that the number of Orowan loops stored around a precipitate is precipitate size dependent, i.e. they are more stable around a large precipitate compared to a smaller one. The following expression for n as a function of plastic strain is thus obtained:

$$n = n^* \left(1 - \exp\left(-\frac{2rM}{bn^*} \varepsilon_p\right)\right). \quad (6)$$

The dislocation density stored around precipitates ρ_p is expressed as the product of the number of loops efficiently stored around one precipitate $n\phi$, the precipitate density $3f_v/4\pi r^3$ and the length of a loop stored around a precipitate $2\pi r$, i.e.:

$$\rho_p = n\phi \frac{3f_v}{2r^2}. \quad (7)$$

Therefore the present model for strain hardening includes two state variables: the statistical dislocation density ρ_s and the number of loops stored around a precipitate n .

- The isotropic contribution to strain hardening σ_{iso} can be expressed as [11]:

$$\sigma_{iso} = \alpha GbM \sqrt{\rho_s + \rho_p}. \quad (8)$$

- The kinematic contribution to strain hardening σ_{kin} can be expressed based on Eshelby's solution giving the average stress in the precipitate [40] as:

$$\sigma_{kin} = f_v E_p \varepsilon_p^*, \quad (9)$$

where E_p is the Young's modulus of the precipitate and ε_p^* is the unrelaxed plastic strain associated with the formation of an Orowan loop around the precipitate. For spherical particles of radius r , the unrelaxed plastic strain can be expressed as [35]:

$$\varepsilon_p^* = \frac{\phi nb}{2rM}. \quad (10)$$

Note that the original expression by Brown and Stobbs [35] has been modified to account for the efficiency of dislocation storage ϕ .

The prediction of the flow stress also requires the prediction of the initial yield stress σ_y that is composed of the contribution of the lattice friction and the Hall–Petch effect σ_0 , the contribution of the solid solution $\sigma_{ss} = K \cdot C_{ss}^{2/3}$ (where C_{ss} is the total solid-solution content expressed in at.% and K is a constant) and the contribution of the precipitates σ_p , which is calculated as:

$$\sigma_p = \sigma_y - \sigma_0 - \sigma_{ss}, \quad (11)$$

where σ_y is the measured initial yield strength. The power law of the contribution of solute atoms is the standard Friedrich Haasen theory [61]. The linear additivity rule is proposed here for simplicity but its validity is still a matter of debate (see recent paper by Dong et al. [62]). The choice of a linear additivity rule is supported by the very different spacing and strengths of the various contributions (solute atoms and precipitates) as explained, for example, by

Brown and Ham [63], Ardell [64], Kocks et al. [37] and Dong et al. [62]. Nevertheless, the choice of additivity rule for determining the strength contribution of the precipitates has a limited impact on the strain-hardening capacity predictions. Note that the values of σ_y used in the model were increased by $\Delta\sigma_y$ compared to the 0.02 offset of plasticity from Fig. 6a for the slightly over-aged samples in order to bypass the elastoplastic transition not described in the present model. For the M21h, M45h and T7651 samples, $\Delta\sigma_y$ is 18, 10 and 10 MPa, respectively. σ_p could also have been calculated using the expression provided in Ref. [65] but here we choose to limit the errors involved in coupling models and preferred to use the experimental expression of the initial yield stress σ_y to calculate σ_p .

As dislocations and precipitates have different densities but the same order of magnitude in strength, a quadratic addition law must be considered between the hardening contributions of the precipitates σ_p and the strain hardening by dislocations σ_{iso} , in agreement with the classical theory [37] and with recent numerical simulations above approximately 0.1% of plastic strain (corresponding to ~0.3% of plastic shear strain) [18]. However, a linear addition applies to the kinematic contribution to strain hardening. In the case of a simple tensile test, the flow stress is finally given by:

$$\begin{aligned}\sigma_f &= \sigma_0 + \sigma_{ss} + \sigma_{kin} + \sqrt{\sigma_p^2 + \sigma_{iso}^2} \\ &= \sigma_0 + \sigma_{ss} + f_v E_p \frac{bn\phi}{2rM} \\ &\quad + \sqrt{\sigma_p^2 + \left(\alpha G b M \sqrt{\rho_f + n\phi} \frac{3f_v}{2r^2}\right)^2},\end{aligned}\quad (12)$$

where n is given by Eq. (5), σ_p is given by Eq. (11), and ρ_f is obtained by solving Eq. (2) combined with Eq. (4).

5.2. Modelling uniaxial tensile tests

Table 1 presents the parameters of the strain-hardening model for the AA7449 alloy. The only tuneable parameters are n^* , M , α and y_p and they are found in the expected range. Note in particular that $n^* = 9$ is much lower for this 7xxx alloy compared to the $n^* = 60$ found by Proudhon et al. [40] who studied a 6xxx series alloy. This is, however, expected due to the difference in shape between the ellipsoidal-shaped η precipitates found in over-aged 7xxx and the very long needle-shaped β' precipitates found in over-aged 6xxx series alloys, capable of holding more Orowan loops. k_1 and k_2^0 are supposed constant and calculated from the dislocation storage rate θ_0 and dynamic recovery rate β_0 (see Eq. (3)) at peak strength where they are minimum, i.e. θ_{0-min} and β_{0-min} . The annihilation distances y_0 and y_p , given in Table 1, allow us to calculate $k_2^0 = 2y_0/b = 2\beta_{0-min}/M$ and $k_2^p = 2y_p/b$.

Fig. 11 shows good agreement between the experimental and predicted stress–strain curves for over-aged conditions. Contrary to the paper of Simar et al. [5], under-aged conditions have not been considered, neglecting in that way dynamic precipitation affecting mainly θ_0 in under-aged conditions.

The predicted evolution of $\theta = d\sigma/d\varepsilon$ with stress is not linear but an attempt to extract a mean value for the slope β_0 and the initial value θ_0 is presented in Fig. 6 together with the experimental data. The model correctly predicts the dislocation storage rate θ_0 and the dynamic recovery rate β_0 in the slightly over-aged temper but foresees a decrease of those parameters in the most over-aged tempers (the one with precipitates above the critical radius for loss of coherency), which is not explicitly observed experimentally for this alloy but was observed by Simar et al. [5] for a 6005A alloy.

Table 1
Parameters of the yield strength and strain-hardening model.

Parameter	Significance	Value	Origin
b	Burgers' vector	0.284 nm	–
G	Matrix shear modulus	27 GPa	–
M	Taylor's factor	2	Anisotropic material
n^*	Maximum number of loops around a precipitate	9	Fitted on exp. σ – ε curves
R_{trans}	Precipitate shearing/bypassing transition radius	3.3 nm**	SAXS measurements
R_{trans2}	Precipitate coherency/incoherency transition radius	15 nm	Fitted on exp. σ – ε curves
E_p	Precipitate's Young modulus	59 GPa	[54]
α	Parameter of the Taylor law	0.2	Fitted on exp. σ – ε curves
θ_{0-min}	θ_0 if no Orowan loops are stored	974 MPa	Tensile test at peak strength
y_0	Annihilation distance between two moving dislocations	0.6 nm	Tensile test at peak strength
y_p	Annihilation distance between two moving dislocations helped by an Orowan loop	10 nm	Fitted on σ – ε curves
σ_0	Stress contribution of Hall–Petch	39 MPa	[55]
K	Parameter of the solid solution contribution to strength	805 MPa/at.% ^{2/3}	Fitted on exp. σ_y
ρ_0	Initial dislocation density	10^{12} m^{-2}	Assumed

** Note that for the calculation of ϕ , R_{trans} is reduced by 20% to allow a better description of the experimental results for low heat treatment times (sample SART, 21h).

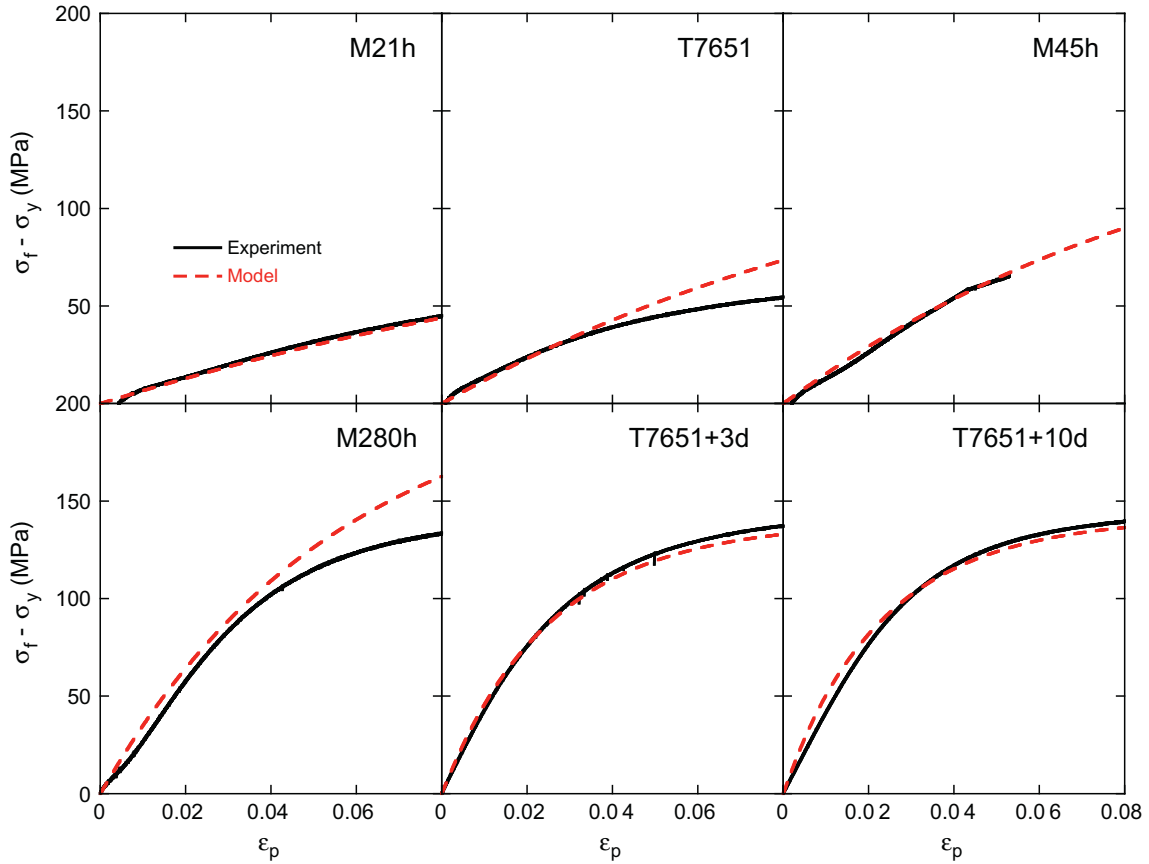


Fig. 11. Experimental vs. modelled stress–strain curves, represented after the yield stress.

5.3. Modelling the Bauschinger test

The kinematic contribution to strain hardening is shown in Fig. 8 together with the experimental results for the internal stress. This value should correspond to the steady-state internal stress, since we have evidenced that the flow stress at small reverse plastic strains was mainly governed by the reversibility of plastic flow. There is actually a reasonable agreement between the evolution of kinematic hardening with forward plastic strain and the measured internal stress for the largest values of reverse plastic strain.

As for the transient behaviour, due to the OHRB, the yield stress contribution evolves during the Bauschinger tests. During the forward stage, the flow stress is the sum of the yield stress, the isotropic contribution and the kinematic contribution. During the reverse loading, the contribution of the precipitates to the flow stress is expected to be lower than during the forward loading since some precipitates are looped by dislocations. Provided that the glide proceeds via the same path, these loops will make the precipitate inefficient at pinning dislocations moving backwards (see Section 4.2). The detailed analysis of this phenomenon is beyond the scope of the present paper, and we propose a phenomenological approach: only a proportion $1 - \chi$ of the precipitates will experience the OHRB,

and therefore the precipitate contribution to the reverse flow stress should be multiplied by χ (Eq. (14)):

$$\begin{aligned} \sigma_f^{\text{Forward}} &= \sigma_o^* + \sigma_{\text{kin}} + \sqrt{\sigma_p^2 + \sigma_{\text{iso}}^2} \quad \text{where } \sigma_o^* \\ &= \sigma_o + \sigma_{\text{ss}} \end{aligned} \quad (13)$$

$$\sigma_f^{\text{Reverse}} = \sigma_o^* - \sigma_{\text{kin}} + \sqrt{(\chi\sigma_p)^2 + \sigma_{\text{iso}}^2} \quad (14)$$

$\chi \in [0; 1]$ therefore accounts for the reversibility of the strain path as well as the proportion of the Orowan loops stored around the dislocations. The Bauschinger stress as measured on Fig. 7 and reported in Fig. 8 is therefore not equal to the true kinematic strain-hardening contribution σ_{kin} , but to:

$$\begin{aligned} 2\sigma_B = \Delta\sigma &= \sigma_f^{\text{Forward}} - \sigma_f^{\text{Reverse}} \\ &= 2\sigma_{\text{kin}} + \sqrt{\sigma_p^2 + \sigma_{\text{iso}}^2} - \sqrt{(\chi\sigma_p)^2 + \sigma_{\text{iso}}^2}. \end{aligned} \quad (15)$$

If one makes the reasonable approximation that $\sigma_{\text{iso}} \ll \sigma_p$ and $\sigma_{\text{iso}} \ll \chi\sigma_p$, Eq. (15) reduces to:

$$\sigma_B \approx \sigma_{\text{kin}} + \frac{\sigma_p}{2}(1 - \chi). \quad (16)$$

Predicting the value of χ as a function of microstructure is a difficult question that reflects the collective behaviour of dislocations. It probably depends on the density of Orowan loops (which depends on both the density and size

Table 2
Evaluated value of the χ parameter for each temper.

Temper	M21h	T7651	M45h	M280h	T7651 + 3d	T7651 + 10d
χ	0.29	0.25	0.28	0.23	0.08	~0

of non-shearable precipitates and on the strain), as well as on the interactions between mobile dislocations and obstacles. It also certainly depends on the intrinsic ability of dislocations for changing planes and thus having irreversible back and forth motions. Discrete dislocation simulations should help to shed some light on the parameters controlling χ . Recent work has shown that it is a powerful tool for investigating collective effects of precipitation hardening during strain reversal [66].

However, it is possible at this stage to determine χ empirically for each case. To extract χ from Eq. (16), values for σ_B and σ_{kin} are required. σ_{kin} is given by the model (Eq. (9)). σ_B is given by the Bauschinger test results presented in Fig. 8 for a forward plastic strain of 0.01, in order to remain in a case where plastic flow is at least partly reversible (see Fig. 9c and associated discussion in Section 4.2), and a reverse plastic strain of 0.01, in order to capture the OHRB phenomenon. The result is shown in Table 2 for various tempers. The low values of χ prove that the dislocation path is partly reversible and that the dislocation loops stored during the forward stage are recovered by the mobile dislocations in the early stages of strain reversal degrading the apparent flow stress. χ decreases with increasing precipitate radius, more evidently when comparing slightly over-aged samples with massively over-aged samples. This is consistent with the qualitative explanation given in Section 4.2. Large precipitates do store Orowan loops more efficiently than small ones, and the Orowan loops stored around large precipitates are expected to be more stable with respect to cross-slip, which favours the reversibility of plastic flow.

6. Conclusions

In this paper we have developed a microstructure-based model for the strain hardening of precipitation-hardened materials that describes both the isotropic and kinematic contributions to flow stress evolution. This model has been tested against a wide variety of microstructures in a 7000 series Al alloy ranging from the peak strength of this material to massively over-aged states. It is capable of describing the strain-hardening behaviour during forward plastic strain, as well as the saturation internal stress during reverse straining (Bauschinger effect). It is based on the KME formalism, and includes a number of additional ingredients such as the efficiency of dislocation loop storage as a function of precipitate size and the influence of precipitate spacing on dynamic recovery.

Furthermore, we propose that the Bauschinger effect at small reverse plastic strains is controlled by the annihilation of stored Orowan loops by reverse gliding disloca-

tions, which reduces the precipitation-strengthening contribution during the first stages of reverse plastic strain. The magnitude of this effect that we call Orowan loop helped reverse bypass (OHRB) has been evaluated for different microstructures, and discussed in terms of the reversibility of plastic flow.

Additional progress in the understanding of strain-hardening requires work in several directions. In terms of the modelling of monotonous straining, the effect of non-shearable particles is now reasonably well described. However, the situation is much less clear with respect to shearable precipitates, as the strain hardening depends in a complex way on the effect of the remaining solute (whose influence on strain hardening is not yet properly understood), on the effect of precipitate shearing on subsequent strain hardening, on the plastic glide patterning (localization and pile ups) that can modify the kinematic hardening contribution, and on the possible strain-induced evolution of precipitate microstructures (dissolution or dynamic formation). In terms of the understanding of strain reversal, we believe that an effort should be now made to predict the reversibility of the dislocation motion as a function of the microstructure and the straining parameters (forward and reverse plastic strain).

Acknowledgements

The staff of BM02-D2AM beamline of ESRF is thanked for technical help with the synchrotron experiments. This work was carried out in the COMPACT project which is a collaboration between Airbus UK (Project Co-ordinator), Alcan—Centre de Recherches de Voreppe, Limerick University, University of Bristol, Enabling Process Technologies, University of Hannover, EADS Germany, University of Patras, Alenia Aeronautica, Ultra RS, Institut Polytechnique de Grenoble and the University of Sheffield. The project was jointly funded by the European Union Framework 6 initiative and the project partners. A.D. wishes to acknowledge the support of the European Research Council for support in the framework of the NEMOLight Marie Curie International Outgoing Fellowship within the 7th European Community Framework Programme. A.S. is a post-doctoral fellow of the FRS-FNRS, Belgium. A.S. also acknowledges the financial support of the HetMat network and the Belgian Interuniversity Attraction Poles (IAP) P6/24.

References

- [1] Gil Sevillano J. Flow stress and work hardening. In: Cahn RW, Haasen P, Kramer EJ, editors. Material science and technology: a comprehensive treatment, vol. 6; 1993. p. 19–88.
- [2] Kocks U, Mecking H. Prog Mater Sci 2003;48:171–273.
- [3] Park D, Niewczas M. Mater Sci Eng A 2008;491:88–102.
- [4] Cheng L, Poole W, Embury J, Lloyd D. Metall Mater Trans A 2003;34A:2473–81.
- [5] Simar A, Bréchet Y, de Meester B, Denquin A, Pardoën T. Acta Mater 2007;55:6133–43.

- [6] Fazeli F, Poole W, Sinclair C. *Acta Mater* 2008;56:1909–18.
- [7] Royset J, Ryum N, Bettella D, Tocco A, Jia Z, Solberg J, et al. *Mater Sci Eng A* 2008;483–484:175–8.
- [8] da Costa Teixeira J, Bourgeois L, Sinclair C, Hutchinson C. *Acta Mater* 2009;57:6075–89.
- [9] Sharma V, Sree Kumar K, Nageswara Rao B, Pathak S. *Metall Mater Trans A* 2009;40:3186–95.
- [10] Westermann I, Hopperstad OS, Marthinsen K, Holmedal B. *Mater Sci Eng A* 2009;524:151–7.
- [11] Myhr OR, Grong Ø, Pedersen KO. *Metall Mater Trans A* 2010;41:2276–89.
- [12] Esmaeili S, Cheng LM, Deschamps A, Lloyd DJ, Poole WJ. *Mater Sci Eng A* 2001;319–321:461–5.
- [13] Rodney D. *Acta Mater* 2004;52:607–14.
- [14] Chen Z, Kioussis N, Ghoniem N. *Phys Rev B* 2009;80:184104.
- [15] Osetsky Y, Bacon D. *Philos Mag* 2010;90:945.
- [16] Proville L, Bakó B. *Acta Mater* 2010;58:5565–71.
- [17] Shin CS, Fivel MC, Verdier M, Oh KH. *Philos Mag* 2003;83:3691–704.
- [18] Queyreau S, Monnet G, Devincere B. *Acta Mater* 2010;58:5586–95.
- [19] Devincere B, Kubin L. *C R Phys* 2010;11:274–84.
- [20] Kocks UF. *J Eng Mater Technol* 1976;98:76.
- [21] Mecking H, Kocks UF. *Acta Metall* 1981;29:1865–75.
- [22] Estrin Y, Mecking H. *Acta Metall* 1984;32:57–80.
- [23] Estrin Y. *Unified constitutive laws for plastic deformation*. New York: Academic Press; 1996.
- [24] Taylor G. *Proc Roy Soc A* 1934;145:362.
- [25] Voce E. *Acta Metall* 1955;51:219.
- [26] Deschamps A, Brechet Y, Necker CJ, Saimoto S, Embury JD. *Mater Sci Eng A* 1996;A207:143–52.
- [27] Bloom T, Kocks U, Nash P. *Acta Metall* 1985;33:265.
- [28] Zolotarevsky N, Solonin A, Chryumov A, Zolotarevsky V. *Mater Sci Eng A* 2009;A502:111–7.
- [29] Kocks U. *Metall Mater Trans A* 1985;A16:2109.
- [30] da Costa Teixeira J, Brechet Y, Estrin Y, Hutchinson C. In: *Proceedings ICAA 12, Yokohama, Japan*. Japan Institute of Light Metals; 2010. p. 536–41.
- [31] Deschamps A, Esmaeili S, Poole WJ, Militzer M. *J Phys IV* 2000;10. Pr6/151–6.
- [32] Pink E. *Acta Metall* 1989;37:1773.
- [33] Deschamps A, Bley F, Livet F, Fabregue D, David L. *Philos Mag* 2003;83:677–92.
- [34] Deschamps A, Niewczas M, Bley F, Brechet Y, Embury JD, Le Sinq L, et al. *Philos Mag A* 1999;79:2485–504.
- [35] Brown L, Stobbs W. *Philos Mag* 1971;23:1185.
- [36] Ashby M. *Philos Mag* 1970;21:399.
- [37] Kocks UF, Argon AS, Ashby MF. *Prog Mater Sci* 1975;19:1.
- [38] Delvalle J, Picasso A, Romero R. *Acta Mater* 2003;51:6443–52.
- [39] Brechet Y, Louchet F. *Acta Metall* 1989;37:2469–73.
- [40] Proudhon H, Poole WJ, Wang X, Bréchet Y. *Philos Mag* 2008;88:621–40.
- [41] Poole W, Embury J, Lloyd D. *Work hardening in aluminium alloys*. In: Lumley R, editor. *Fundamentals of aluminium metallurgy, production, processing and applications*. Cambridge: Woodhead Publishing; 2011.
- [42] Simar A, Brechet Y, de Meester B, Denquin A, Gallais C, Pardoën T. *Prog Mater Sci*, submitted for publication.
- [43] Wilson D. *Acta Metall* 1965;13:807.
- [44] Moan G, Embury J. *Acta Metall* 1979;27:903.
- [45] Warner T. *Mater Sci Forum* 2006;519–521:1271–8.
- [46] Guyot P, Cottignies L. *Acta Mater* 1996;44:4161–7.
- [47] Dumont M, Lefebvre W, Doisneau Cottignies B, Deschamps A. *Acta Mater* 2005;53:2881–92.
- [48] Deschamps A, De Geuser F. *J Appl Crystallogr* 2011;44(Part 2): 343–52.
- [49] Marlaud T, Deschamps A, Bley F, Lefebvre W, Baroux B. *Acta Mater* 2010;58:248–60.
- [50] Lendvai J, Honyek G, Kovacs I. *Scripta Metall* 1979;13:593.
- [51] Mukhopadhyay AK, Yang QB, Singh SR. *Acta Metall* 1994;42:3083.
- [52] Ungar T, Honyek G. *Cryst Res Technol* 1985;20:527.
- [53] Deschamps A, Brechet Y, Guyot P, Livet F. *Z Metallkd* 1997;88:601–6.
- [54] Lendvai J. *Mater Sci Forum* 1996;217–222:43–56.
- [55] Poole W, Wang X, Lloyd D, Embury JD. *Philos Mag* 2005;85:3113–35.
- [56] Stoltz R, Pelloux R. *Metall Mater Trans A* 1976;7A:1295.
- [57] Gould D, Hirsch P, Humphreys F. *Philos Mag* 1974:1351.
- [58] Gerold V. *Precipitation hardening*. In: *Dislocations in solids*, vol. 4. Amsterdam, North Holland; 1979. p. 219.
- [59] Sinclair C, Poole W, Brechet Y. *Scripta Mater* 2006;55:739–42.
- [60] Bouaziz O, Bréchet Y. *Scripta Mater* 2009;60:366–8.
- [61] Haasen P. In: *Nabarro FRN, editor. Dislocations in solids*, vol. 4. Amsterdam, North Holland; 1979 [chapter 15].
- [62] Dong Y, Nogaret T, Curtin W. *Metall Mater Trans A* 2010;41:1954–60.
- [63] Brown L, Ham R. *Strengthening methods in crystals*. London: Applied Science Publishers; 1971.
- [64] Ardell A. *Metall Mater Trans A* 1985;16:2131–65.
- [65] Deschamps A, Brechet Y. *Acta Mater* 1999;47:293–305.
- [66] Queyreau S, Devincere B. *Philos Mag Lett* 2009;89:419–30.